Available online at www.sciencedirect.com
ScienceDirect
Trans. Nonferrous Met. Soc. China 35(2025) 1875−1889
Transactions of Nonferrous Metals Society of China
www.tnmsc.cn

Effect of gradient nanostructures induced by supersonic fine particle bombardment on microstructure and properties of Ni−W−Co−Ta medium-heavy alloy

Yi XIONG[1,2], Miao-miao YANG[1], Nan DU[3], Yong LI[4], Jin-jin TANG[1], Kang-hao SHU[5], Shu-bo WANG[6], Feng-zhang REN[1]

1. School of Materials Science and Engineering, Henan University of Science and Technology, Luoyang 471023, China;
2. Provincial and Ministerial Co-construction of Collaborative Innovation Center for Non-ferrous Metal New Materials and Advanced Processing Technology, Luoyang 471023, China;
3. Luoyang Optoelectronic Technology Development Center, Luoyang 471003, China;
4. Research Institute of Special Steels, Central Iron and Steel Research Institute Company Limited, Beijing 100081, China;
5. CITIC Heavy Industries Co., Ltd., Luoyang 471039, China;
6. Nano and Molecular Systems Research Unit, University of Oulu, Oulu, FIN-90014, Finland

Received 11 October 2023; accepted 3 June 2024

Abstract: The effects of gradient nanostructures induced by supersonic fine particle bombardment (SFPB) on the surface integrity, microstructural evolution, and mechanical properties of a Ni−W−Co−Ta medium-heavy alloy (MHA) were systematically investigated. The results show that gradient nanostructures are formed on the surface of Ni−W−Co−Ta MHA after SFPB treatment. At a gas pressure of 1.0 MPa and an impact time of 60 s, the ultimate tensile strength and yield strength of the alloy reached the maximum values of 1236 MPa and 758 MPa, respectively, which are 22.5% and 38.8% higher than those of the solid solution treated alloy, and the elongation (46.3%) is close to that of the solid solution treated alloy, achieving the optimal strength–ductility synergy. However, microcracks appear on the surface with excessive gas pressure and impact time, generating the relaxed residual stress and decreased strength. With the increase of the impact time and gas pressure, the depth of the deformation layer and the surface microhardness gradually increase, reaching the maximum values (29 μm and HV 451) at 1.0 MPa and 120 s. The surface grain size is refined to a minimum of 11.67 nm. Notably, SFPB treatment has no obvious effect on elongation, and the fracture mode changes from the ductile fracture before treatment to ductile–brittle mixed fracture after treatment.

Key words: supersonic fine particle bombardment; gradient nanostructure; Ni−W−Co−Ta medium-heavy alloy; microstructure; mechanical properties

1 Introduction

Tungsten heavy alloys (WHAs) have a unique combination of properties that make them ideal for various applications, such as aerospace, drilling tools, sports, and the nuclear industry. These properties include high density, superior mechanical strength, excellent stiffness, and commendable oxidation and corrosion resistance [1−3]. However, the tungsten reserves in the world are only 3.7×10^6 t [4], which restricts the mass production and the popularization of WHAs. Therefore, YE et al [5] abandoned the design concept of lightweight alloys

Corresponding author: Yi XIONG, Tel: +86-13526917962, E-mail: xiongy@haust.edu.cn
https://doi.org/10.1016/S1003-6326(25)66788-4

with high W content (greater than 90%) and created medium-heavy alloys (MHAs) with medium W content (50%−75%) because the difference in mechanical properties was negligible. Traditional high-density alloys (WHAs and MHAs) are fabricated by powder metallurgy, which have high porosity and weak interface bonding between the two phases, resulting in poor strength and toughness.

Given these challenges, our research team has transitioned from traditional powder metallurgy preparation methods to an innovative approach using melting, casting and forging processes to synthesize the novel Ni−W−Co−Ta MHA [6]. The high-density tungsten (ρ=19.35 g/cm^3) is used as the solid solution strengthening phase to improve the density and strength of the alloy. Nickel with typical face-centered cubic structure is selected as the matrix. Due to the excellent solubility of tungsten in nickel (up to 32% at 800 °C) and a large number of slip systems in nickel, the problem of being vulnerable to concentrated stress and adiabatic shear bands can be avoided. In addition, the addition of tantalum and cobalt promotes the formation of precipitated phase and the strengthening of fine grains in the alloy. Compared with MHA and WHA prepared by powder metallurgy, the MHA has higher strength and impact toughness. Further studies have shown that the strength of the alloy can be greatly improved by pre-deformation and subsequent aging treatment [7]. However, the issue related to the strength−toughness paradigm remains. Therefore, it is very important to determine a robust process to improve the comprehensive mechanical properties of MHA.

A large number of studies have shown that heterogeneous architectural design can effectively alleviate the strength−ductility tradeoff of the conventional metallic materials [8]. Therefore, materials scientists have developed various methods for inducing heterostructures [9]. Among them, the construction of gradient nanostructures has become one of the most straightforward and feasible methods [10−15]. This is because the gradient nanostructures can effectively inhibit the localization of strain, thus significantly increasing the strength of the metals while maintaining a fairly high ductility [12]. In addition, these nanostructures have been shown to improve the fatigue life, wear resistance and other key properties of materials. Gradient nanostructures are usually prepared by surface nanocrystallization technology, such as the ultrasonic surface rolling process [16], laser shock peening [17], high-energy shot blasting [18], ultrasonic shock treatment [19], and surface mechanical attrition treatment [20]. Although these technologies are effective, they are often limited by expensive infrastructure and operating costs, as well as by the limitations of handling large size or complex geometric parts, making them unsuitable for industrial mass production [21,22].

In contrast, the supersonic fine particle bombardment (SFPB) has emerged as a more advanced and efficient technology that greatly expands the capabilities of traditional shot peening. SFPB is carried out with recyclable solid particles, enabling cost-effective processing of large and complex structural parts [23,24]. More importantly, it has been widely applied to various materials [25−28]. For example, MA et al [25] used SFPB to achieve nanocrystallization on the surface of 1Cr−18Ni−9Ti austenitic stainless steel. At the same time, martensitic transformation is induced by the deformation of the surface structure, and the wear resistance of the material is significantly improved. LI et al [26] studied the effect of SFPB gas pressure on the surface integrity of DZ2 steel and found that SFPB induced nano-scale refinement of surface grains. In addition, with the increase of gas pressure, the surface roughness is gradually stabilized, the deformation layer depth and microhardness are also gradually increased. It is worth mentioning that our previous research has shown that the strength, corrosion resistance, and fatigue properties of 300M steel [29], TC11 alloy [30], Ti80 alloy [31] and other materials prepared by SFPB have been significantly improved.

However, the current research has mainly concentrated on low-density metals and alloys, with little attention devoted to WHAs and their alternatives (MHAs). Therefore, the present study aimed to apply SFPB treatment to the Ni−W−Co−Ta MHA pioneered by our group. The effects of the SFPB gas pressure and the impact duration on the surface integrity, microstructure, and mechanical properties of this newly developed MHA were systematically investigated to provide an empirical and theoretical basis for the robust engineering of MHAs with optimized properties to replace the costly WHAs in industrial settings.

2 Experimental

The Ni−W−Co−Ta MHA used in this study had the following composition: 38.53 wt.% W, 5.09 wt.% Co, 0.97 wt.% Ta, with the remainder being Ni. The MHA was homogenized at 1200 °C for 24 h and forged into round rods with a diameter of 70 mm and subsequently air-cooled to room temperature. Then, the MHA billet underwent solid-solution treatment at 1000 °C for 1.5 h, and then oil-cooled to room temperature. Afterwards, tensile specimens were machined from the billet. The dimensions of the tensile specimens are illustrated in Fig. 1. These specimens were subjected to grinding and polishing before SFPB treatment. The SFPB process was performed at room temperature using spherical Al_2O_3 particles with an average particle size of about 40 μm. The carrier gas (air) pressure was 1.0 MPa, and the impact time was 30, 60, 90, and 120 s. For a comparative analysis, the SFPB treatment was additionally performed at gas pressures of 0.5 and 1.5 MPa for an impact time of 60 s. The treated area was the black shaded area (both sides) in Fig. 1. Specifically, the spray distance was 30 mm, and the spraying angle was 90°.

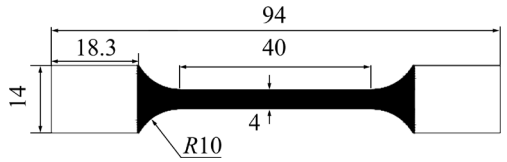

Fig. 1 Dimensions of tensile specimens (thickness of 1 mm) subjected to SFPB treatment (shaded area, both sides) (unit: mm)

The surface topography and roughness (S_a) of the specimens, before and after the SFPB treatment, were characterized using a Nanovea HS1000P three-dimensional profiler. The corresponding surface and cross-section morphologies were observed through a JSM−IT100 scanning electron microscope (SEM) with an electron acceleration voltage of 20.0 kV. Electron backscatter diffraction (EBSD) was also used to analyze the micro-structural evolution of the MHA after SFPB treatment. Transmission electron microscopy (TEM) observations were conducted using a JEM−2100 microscope at an electron acceleration voltage of 200 kV to study the microstructure of the surface and subsurface layers of samples subjected to different SFPB treatments. X-ray diffraction (XRD) was performed using a D8 ADVANCE X-ray diffractometer with a Cu target (wavelength λ=0.154056 nm) at a scanning step of 0.02° and a scanning range of 30°−100°.

For the residual stress measurements, an X-ray stress analyzer (X−350AX) was used with a Cu K_α radiation tube source operating at a voltage of 27 kV and a current of 7 mA. The tube's diameter was 4 mm, and the tilt angles (ψ) were 0°, 15°, 30°, and 45°. An MH−3 microhardness tester was used to characterize the gradient of hardness from the surface to the matrix of the samples, using a loading of 100 g and a dwell time of 10 s. The mechanical properties were determined using an INSTRON 5587 tensile testing machine at a tensile speed of 0.5 mm/min. Finally, the fracture morphologies were observed using a JSM−7800F SEM.

3 Results

3.1 Surface integrity

Figure 2 shows the SEM image and three-dimensional topography of the Ni−W−Co−Ta MHA surface, and the resulting surface roughness (S_a). Prior to SFPB, this MHA has a relatively smooth surface with S_a of only 0.59 μm, which is due to residual traces of mechanically polished stripes (Fig. 2(a)). In the SFPB process, the severe plastic deformation occurs on the specimen surface under the impact of Al_2O_3 particles, resulting in honeycomb impact pits and a substantial increase in S_a (Figs. 2(b−g)). Specifically, when the gas pressure is 1.0 MPa and the impact time is 30 s, the originally smooth surface is covered by micro-pits generated by the bombardment of Al_2O_3 particles. Due to deformation, the surrounding metal material flows and accumulates around these pits, forming local protrusions (Fig. 2(b)). This change causes S_a to rise sharply to 10.15 μm. When the impact time is extended to 60 s, the surface becomes smooth again (Fig. 2(c)) and the S_a decreases to 6.25 μm. This is due to the larger coverage of Al_2O_3 particles during bombardment, which helps to flatten the initially formed protrusions, as shown in Fig. 2(b). When SFPB duration is extended to 90 s, work hardening occurs on the specimen surface, resulting in micro-cracks caused by stress concentration at grain boundaries (Fig. 2(d)) [24,32], and S_a increases

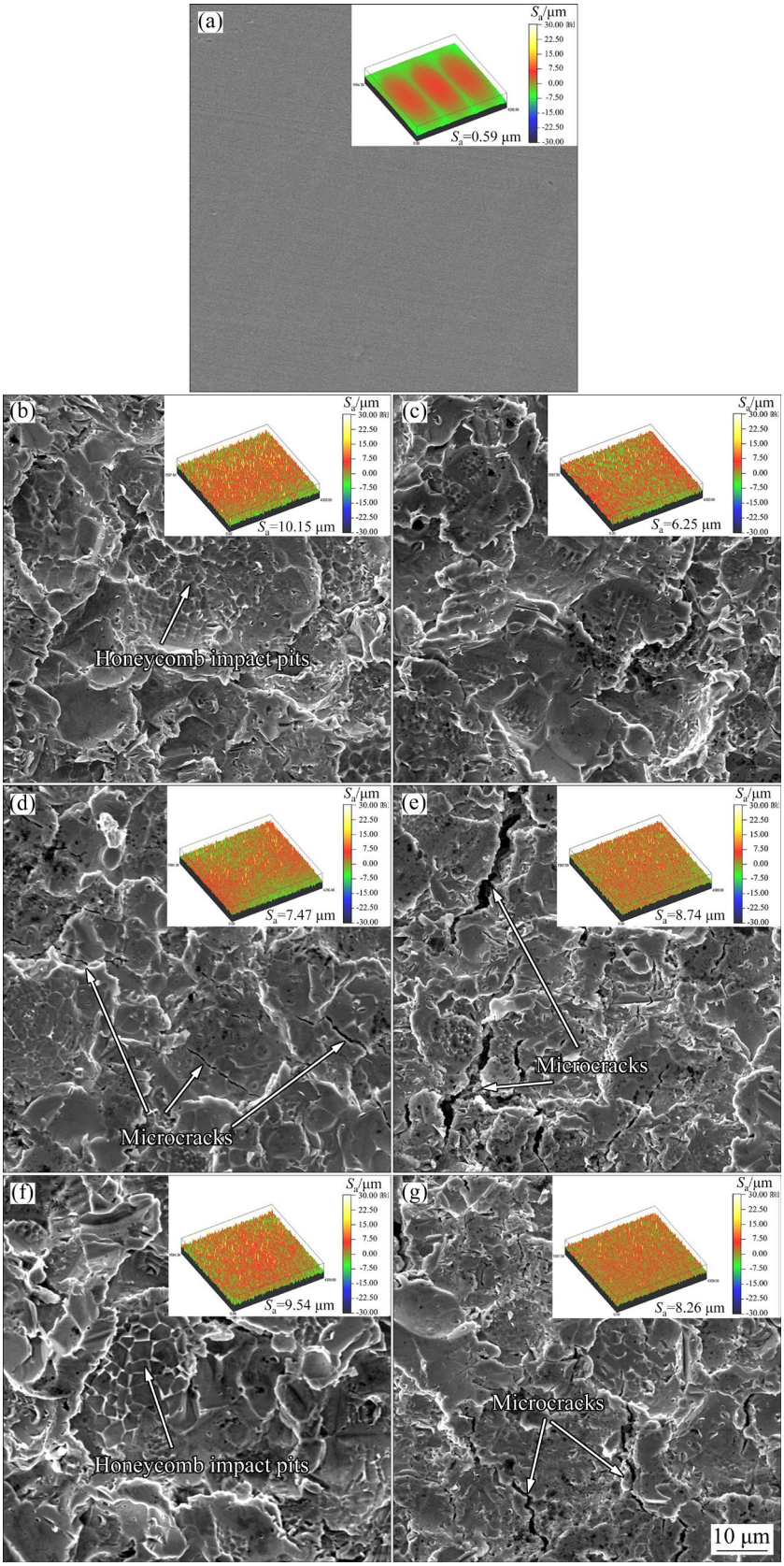

Fig. 2 Two and three-dimensional surface topographies of Ni−W−Co−Ta MHAs before and after SFPB treatment under different conditions: (a) Before SFPB treatment; (b) 1.0 MPa, 30 s; (c) 1.0 MPa, 60 s; (d) 1.0 MPa, 90 s; (e) 1.0 MPa, 120 s; (f) 0.5 MPa, 60 s; (g) 1.5 MPa, 60 s

to 7.47 μm accordingly. When the impact time is extended to 120 s, the surface condition is further deteriorated, the crack expands and widens, and S_a increases to 8.74 μm (Fig. 2(e)).

Notably, S_a demonstrates a similar trend as the gas pressure increases during SFPB, within the same impact duration. For example, at a gas pressure of 0.5 MPa, a large number of micro-pits and honeycomb-like pits appear on the specimen's surface, resulting in S_a of 9.54 μm (Fig. 2(f)). S_a decreases to 6.25 μm at 1.0 MPa, and increase to 8.26 μm at 1.5 MPa, due to the appearance of microcracks at this high-impact kinetic energy (Fig. 2(g)). These observations indicate that both the impact time and gas pressure of SFPB are crucial for manipulating the surface integrity of the alloy. Therefore, it is very important to choose the appropriate SFPB conditions.

3.2 Microstructures

Figure 3 shows the cross-sectional microstructures of the Ni−W−C−Ta MHAs. Before SFPB, the grain boundaries of the alloy can be clearly observed (Fig. 3(a)). In the SFPB process, due to the bombardment of high-energy and high-speed Al_2O_3 particles, the surface layer of the sample undergoes severe plastic deformation. When the gas pressure is 1.0 MPa and the impact time is 30 s, this deformation causes the grain boundary to be unclear, forming a deformation layer with a depth of 16 μm (Fig. 3(b)). The degree of plastic deformation increases with the increase of the impact time, thus increasing the depth of the deformation layer (e.g., 29 μm at 120 s of impact) (Fig. 3(e)). At the same impact time (60 s), the increase of gas pressure significantly increases the kinetic energy transferred by Al_2O_3 particles, and deepens the deformation layer from 15 μm at 0.5 MPa (Fig. 3(f)) to 22 μm (Fig. 3(c)) at 1.0 MPa and 27 μm at 1.5 MPa (Fig. 3(g)).

The representative EBSD analysis reveals a holistic view of the cross-sectional microstructure induced by SFPB in the Ni−W−Co−Ta MHA, as shown in Fig. 4. After SFPB, the gradient structure

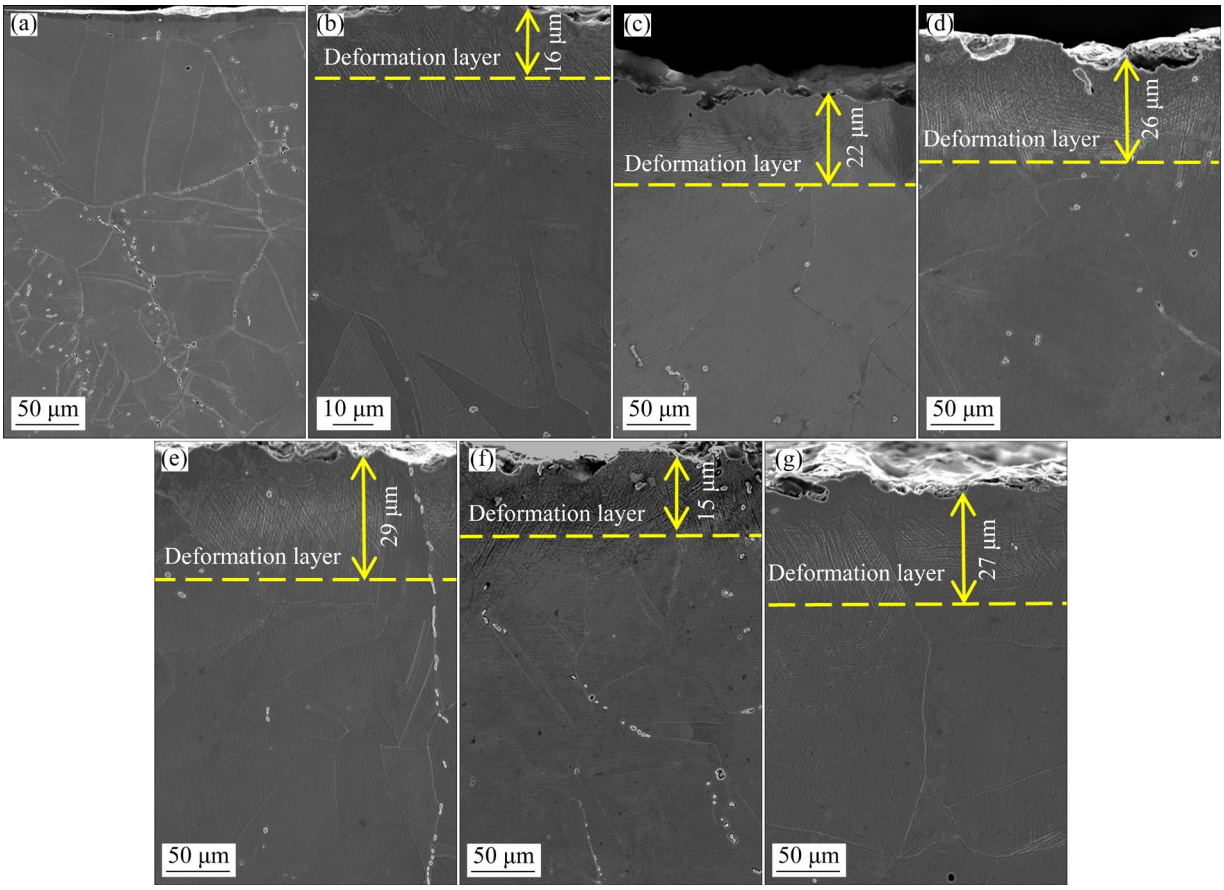

Fig. 3 Cross-sectional microstructures of Ni−W−C−Ta MHAs before and after SFPB treatments under different conditions: (a) Before SFPB treatment; (b) 1.0 MPa, 30 s; (c) 1.0 MPa, 60 s; (d) 1.0 MPa, 90 s; (e) 1.0 MPa, 120 s; (f) 0.5 MPa, 60 s; (g) 1.5 MPa, 60 s

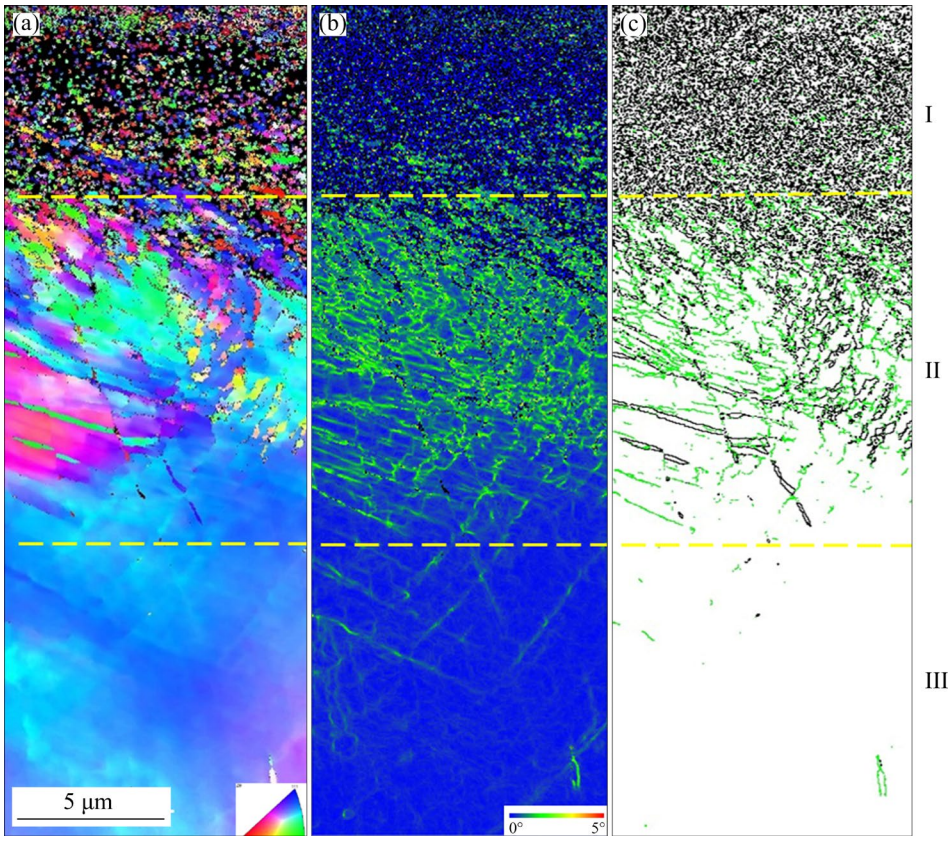

Fig. 4 Representative EBSD maps of Ni−W−Co−Ta MHAs after SFPB treatment at 1.0 MPa and 60 s: (a) Grain orientation map; (b) Map of differences in local orientation; (c) Distribution map of grain boundaries (Solid black and green lines depict high-angle grain boundaries (HAGBs) and low-angle grain boundaries (LAGBs), respectively)

from the surface to the inside can be clearly seen from the grain size (Fig. 4(a)). Deformation level is represented by local orientation difference (Fig. 4(b)) and grain boundary distribution (Fig. 4(c)). The structure can be divided into three regions: Region I is the nanocrystalline surface layer dominated by high-angle grain boundaries (HAGBs); Region II is composed of less deformed subsurface layer and contains more low-angle grain boundaries (LAGBs); Region III represents the undeformed coarse-grained matrix. Regions I and II together form the deformation layer shown in Fig. 3.

The microstructures of MHA surface (Region I in Fig. 4) and subsurface (Region II in Fig. 4) after SFPB treatment are further characterized by TEM, and the resulting images are shown in Fig. 5. When the gas pressure is 1.0 MPa and the impact time is 60 s, the surface grains are seen to have profound fragmentation. This results in a selected area electron diffraction pattern characterized by a continuous ring (Fig. 5(a)), indicating a randomly oriented nanocrystalline state in the surface layer (Region I) of the MHA after SFPB [33]. Using the Nano-Measurer software and truncation method, the corresponding average grain size of (13.44±2.08) nm is determined from the dark field TEM image in Fig. 5(b) (insert Fig. 5(b)). On the other hand, in the subsurface layer (Region II), about 20 μm below the top layer, tangled dislocations and dislocation walls appear due to dislocation diffusion and interaction [34], as shown in Fig. 5(i). When the impact time is extended to 120 s, the degree of fragmentation between surface particles increases significantly (Fig. 5(c)). This reduces the grain size to (11.67±1.94) nm (Fig. 5(d)), further highlighting the continuous annular feature of the selected area electron diffraction pattern in the inset of Fig. 5(c). However, in the subsurface layer, dislocations accumulate, forming dislocation cells (Fig. 5(j)).

Under the condition of constant impact time of 60 s, the influence of gas pressure is compared and analyzed. As shown in Fig. 5(e), at a low pressure of 0.5 MPa, the surface grain is relatively coarse, with a grain size of (14.97±2.35) nm. This results in the formation of discrete diffraction points rather

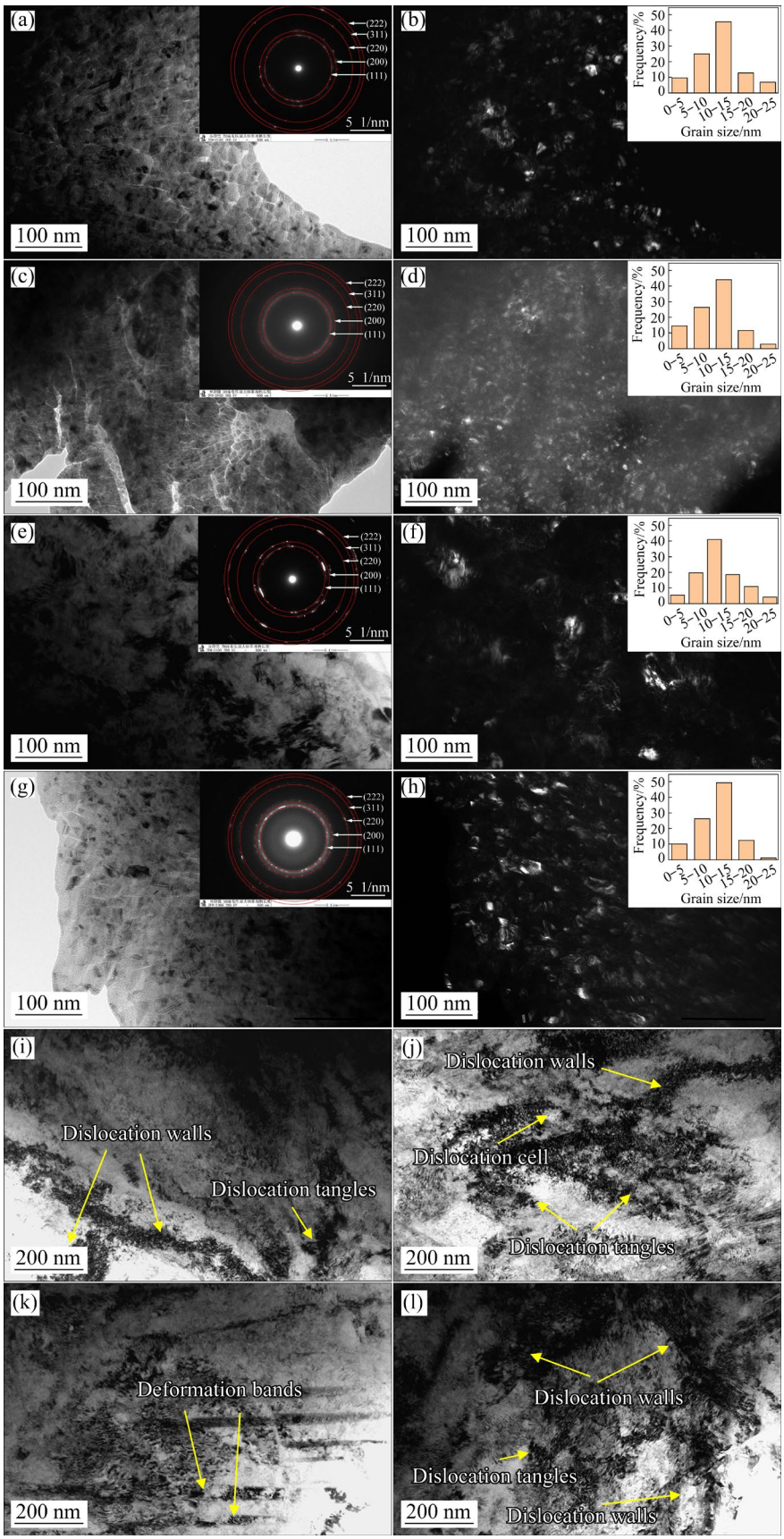

Fig. 5 Bright field (a, c, e, g) and corresponding dark field (b, d, f, h) TEM images for surface layer, and bright field TEM images for subsurface layer (i, j, k, l) of Ni−W−Co−Ta MHAs after SFPB treatments at different gas pressures and impact time: (a, b, i) 1.0 MPa, 60 s; (c, d, j) 1.0 MPa, 120 s; (e, f, k) 0.5 MPa, 60 s; (g, h, l) 1.5 MPa, 60 s

than continuous rings in the electron diffraction pattern of the selected region. At a high pressure of 1.5 MPa (Fig. 5(g)), the microstructure of the surface layer is similar to that at 1.0 MPa, but the grain size is slightly reduced to 11.93 nm. On the contrary, there are obvious differences in the microstructure of the subsurface layer. The observed deformation band harmonizes the relatively low deformation level at 0.5 MPa (Fig. 5(k)). At 1.0 MPa, this microstructure feature disappears in Fig. 5(i). Finally, the dislocation structure, dislocation walls, and entanglement are more complex at 1.5 MPa than at 1.0 MPa, resulting in the formation of dislocation cells (Fig. 5(l)).

The XRD patterns in Fig. 6 show that after SFPB treatment, the main phase of MHA's central face-centered cubic $Ni_{17}W_3$ continues to exist without any new phase. However, a zoomed view of the (111) plane shows that the peak becomes wider and moves to the left at a lower 2θ angle. This phenomenon is often observed in SFPB-treated alloys, such as in Ref. [21], and is mainly caused by grain refinement (Fig. 4) and the accumulation of microstrains in the surface layer. The microstrain is quantified by Williamson−Hall method [30]:

$$\beta\cos\theta=\varepsilon(4\sin\theta)+k\lambda/D \quad (1)$$

where β is the full width at half maximum of the diffraction peaks, θ is the Bragg diffraction angle in rad, ε is the microstrain, k is the Scherrer constant (taken as 0.9), λ is the X-ray wavelength (0.15406 nm), and D is the grain size and taken from the TEM analysis of grain size. The equivalent accumulated dislocation density (ρ) is calculated as [35]

$$\rho=\frac{2\sqrt{3}(\varepsilon^2)^{1/2}}{Db} \quad (2)$$

where b represents the magnitude of Burgers vector. As can be seen from the results in Fig. 7, the microstrain and equivalent accumulated dislocation density gradually increase with the increase of impact time and gas pressure.

3.3 Mechanical properties

Figure 8 shows that Ni−W−Co−Ta MHAs exhibit compressive residual stress (CRS) on the surface after SFPB. Under constant gas pressure of 1.0 MPa, CRS first increases and then decreases with the extension of impact time. When the impact time is 60 s, the peak CRS is 988 MPa. Further extension of the impact time to 120 s results in a large number of microcracks on the surface (Fig. 2(e)), which in turn cause partial release of CRS [36], resulting in a slight decrease in CRS. The variation trend of CRS with gas pressure is similar to that of impact time. Specifically, due to the formation of many microcracks at 1.5 MPa, the CRS is reduced to a minimum of 888 MPa.

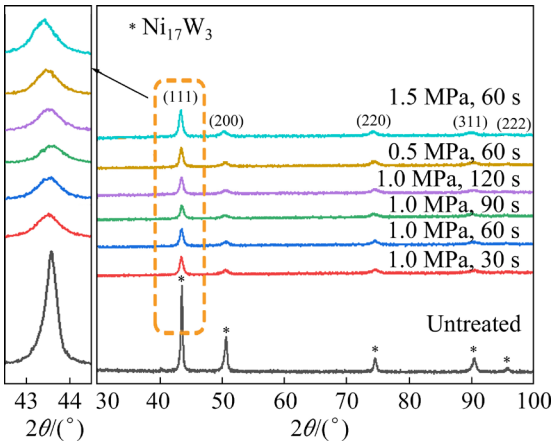

Fig. 6 XRD patterns of Ni−W−Co−Ta MHAs

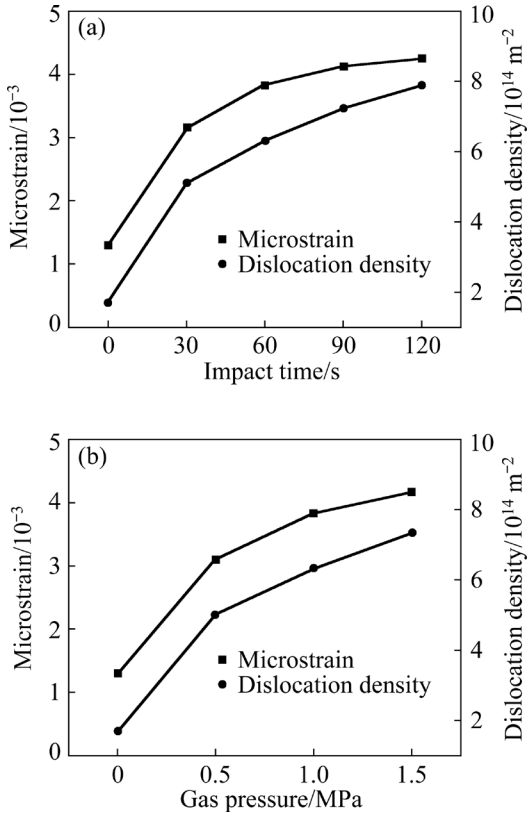

Fig. 7 Dislocation density and microstrain of Ni−W−Co−Ta MHAs as function of impact time (a) and gas pressure (b) of SFPB treatment

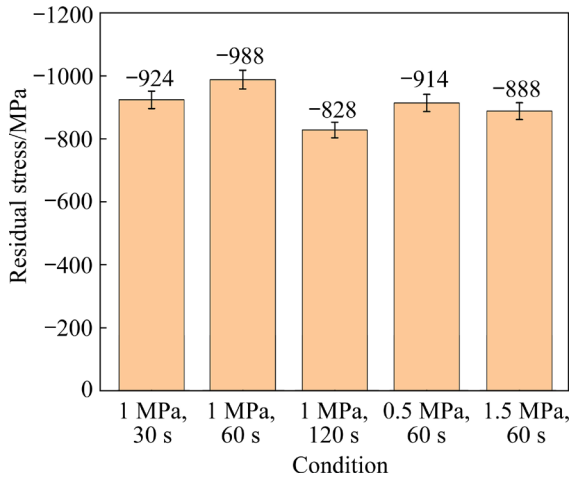

Fig. 8 Surface residual stress of Ni−W−Co−Ta MHAs after SFPB treatment at various gas pressures and impact time

Figure 9 shows the microhardness distribution of the Ni−W−Co−Ta MHAs at different depths. In the initial solid solution state, the microhardness of the alloy remains relatively constant from the surface to the matrix, with an average of about HV 325. After SFPB treatment, the surface microhardness and the depth of the hardened layer are significantly increased. At 1.0 MPa, with the impact time extending from 30 to 120 s, the surface hardness increases from HV 398 to HV 451, and the surface hardness increases by 22.5% and 38.8%, respectively, compared with that of the untreated sample. The hardening layer depth also shows a similar increasing trend (from 40 to 80 μm). When the impact time is kept constant at 60 s, the increase in gas pressure also increases the surface hardness and the depth of the hardened layer. Under the gas pressure of 1.5 MPa, the surface microhardness reaches HV 445 and the depth of the hardened layer reaches 70 μm.

Figure 10 shows the mechanical properties of the Ni−W−Co−Ta MHA. In the solid solution state, the ultimate tensile strength and yield strength of the alloy are 1009 and 546 MPa, respectively, and the elongation is 49.2%. After SFPB treatment, the intensity index of MHA is significantly increased.

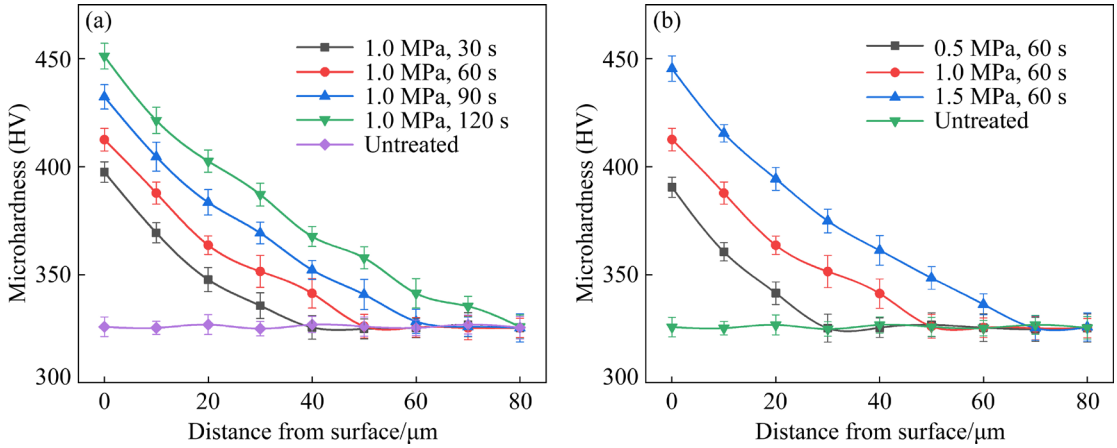

Fig. 9 Microhardness profiles of Ni−W−Co−Ta MHAs across different depths before and after SFPB treatment under different conditions of impact time (a) and gas pressure (b)

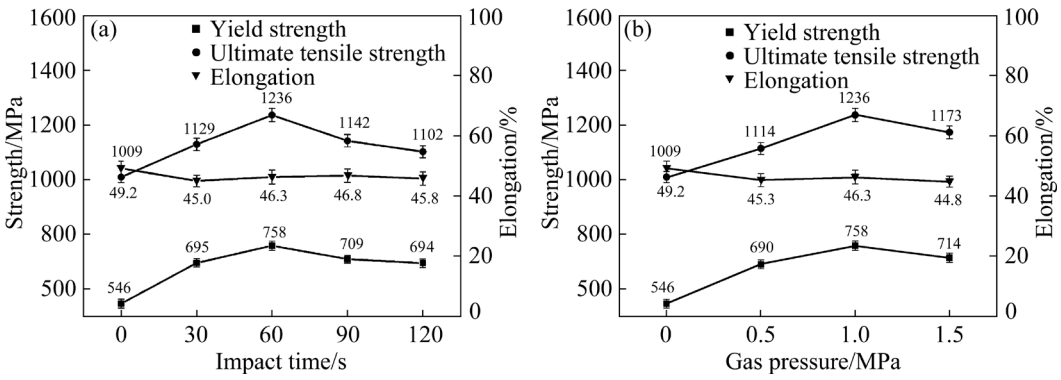

Fig. 10 Mechanical properties of Ni−W−Co−Ta MHA: (a) Effect of impact time of SFPB at gas pressure of 1.0 MPa; (b) Effect of gas pressure of SFPB at impact time of 60 s

When the gas pressure is 1.0 MPa, with the extension of impact time, the ultimate tensile strength and yield strength of the alloy first increase, and reach the peak values of 1236 and 758 MPa at 60 s, respectively, which are 22.5% and 38.8% higher than those without SFPB treatment. However, after 90 s of impact, the appearance of surface microcracks reduces the strength. At the impact time of 120 s, the crack further expands and the corresponding strengths further decrease to 1102 and 694 MPa, respectively (Fig. 10(a)). At constant impact time of 60 s, the variation trend of the strength with the gas pressure is shown in Fig. 10(b). Therefore, the optimal SFPB treatment condition of the Ni−W−Co−Ta MHA is determined to be 1.0 MPa for gas pressure and 60 s for impact time. In addition, it is worth noting that the elongation of MHA after SFPB does not change significantly compared to that of the solid solution specimen. This shows that the gradient layer of the nanostructure formed by SFPB effectively improves the strength without sacrificing plasticity.

After tensile failure, the fracture morphologies of the Ni−W−Co−Ta MHAs are shown in Fig. 11. Prior to SFPB, fractures are mainly characterized by large and deep dimples, indicating ductile fractures (Fig. 11(a)). After SFPB treatment, the fracture surface of the alloy changes significantly, the cleavage surface increases, the proportion of dimple area decreases, and the composite morphologies of quasi-cleavage and ductile fracture are shown in Figs. 11(b−g). In addition, the cleavage area decreases and the proportion of dimples moving inward from the surface increases correspondingly. The cleavage surface mainly appears in the surface deformation layer. Therefore, with increasing impact time, the cleavage plane and the corresponding surface deformation layer deepen (Figs. 11(b−e)). Similarly, an increase in gas pressure leads to a gradual deepening of the cleavage surface and deformation (Figs. 11(f, g)). The observations are in good agreement with the microstructure characteristics shown in Fig. 3.

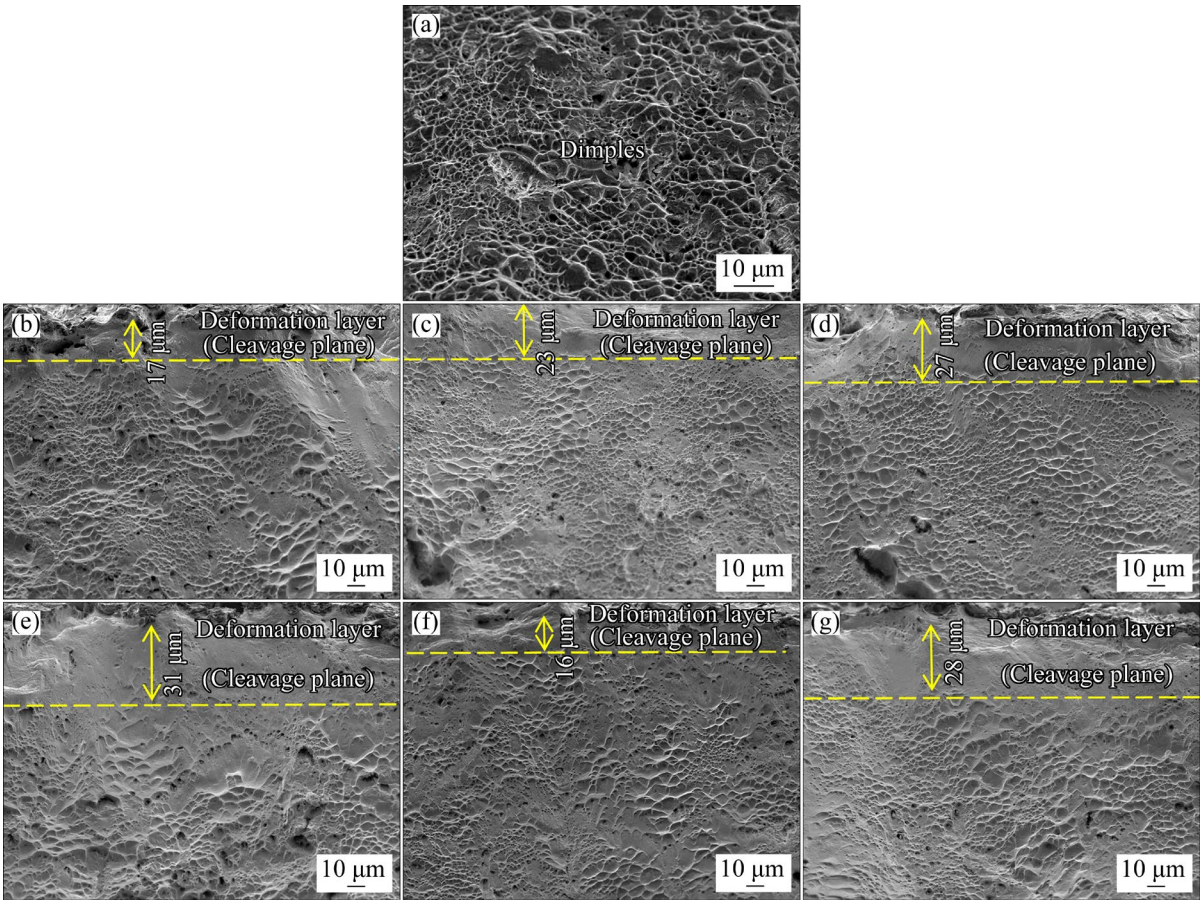

Fig. 11 Tensile fracture morphologies of Ni−W−Co−Ta MHAs before and after SFPB treatment under different conditions: (a) Before SFPB treatment; (b) 1.0 MPa, 30 s; (c) 1.0 MPa, 60 s; (d) 1.0 MPa, 90 s; (e) 1.0 MPa, 120 s; (f) 0.5 MPa, 60 s; (g) 1.5 MPa, 60 s

4 Discussion

4.1 Influence of SFPB treatment on microstructural evolution

By SFPB treatment, a gradient structure with nanocrystalline surface and deformed subsurface is successfully constructed on the surface of the Ni−W−Co−Ta MHA, and the rest is coarse-grained matrix. In terms of surface integrity, SFPB should be optimal at a gas pressure of 1.0 MPa and an impact time of 60 s.

In the SFPB process, high-speed Al_2O_3 particles strongly impact the alloy surface. This leads to an increase in strain rate and strain on the specimen surface, resulting in severe plastic deformation of the surface layer [37] (Fig. 3). TEM observations (Fig. 5) confirm that the alloy coordinates plastic deformation primarily through dislocation motion and interaction. Therefore, the kinetic energy of the impacted Al_2O_3 particles is converted into the deformation energy stored in the sample. An increase in strain rate and strain usually results in an increase in storage dislocation density [38]. This deformation promotes the interaction of the dislocation diffusion and rearrangement, resulting in entangled dislocations and a dense network of dislocation walls. With the continuous accumulation of dislocations, these dislocation entanglements and walls subdivide the grains into cellular substructures with LAGBs [39]. Further increase of strain results in the accumulation of more dislocations at the grain boundaries. This dislocation movement increases the orientation difference between the two sides of the subgrain boundary, gradually transforms the subgrain boundary into HAGBs, and promotes the formation of surface nanocrystals. Through repeated cycles of these processes, the surface grain structure of the alloy is eventually refined to the nanoscale (Figs. 5(b, d, f, h)). As the strain continues, the refined small grains make the dislocation movement more and more difficult, but grain rotation and grain boundary sliding become easier [21,40]. Therefore, to minimize the internal energy of the grains, the nanocrystals rotate on the sample surface to form randomly oriented nanoscale grains (Figs. 5(a, c, e, g)). High density dislocation can also cause surface work hardening [24]. This hardening makes the alloy less able to withstand additional plastic deformation [32], resulting in stress concentration that ultimately leads to the formation of microcracks (Fig. 2(d)) and subsequent propagation (Fig. 2(e)).

The magnitude of deformation gradually decreases from the surface layer to the material and almost no deformation occurs in the core. A similar microstructure response is observed in AISI 316L stainless steel after shot peening [41], which is due to the decrease of strain rate and strain with increasing distance from the surface, thus weakening the overall deformation degree of the sample.

In the SFPB process, the plastic deformation level of the alloy is the highest in the surface layer, because the impact kinetic energy attenuates when entering the matrix from the top layer. The reduction in dynamic strain and strain rate reduces the deformation level [25]. Thus, the subsurface exhibits deformation bands (Fig. 5(k)), followed by dislocation walls and cells (Fig. 5(i)), and then a LAGB-dominated subgrain structure (Fig. 5(l)). Beyond the hardened layer, however, the deeper matrix remains unformed and retains its initial structure (Fig. 3). This gradient structure also creates a microhardness gradient in the depth of the material.

4.2 Influence of SFPB treatment on mechanical properties

The gradient nanostructures constructed on the Ni−W−Co−Ta MHA surface significantly increase the ultimate tensile strength and yield strength of the alloy without adverse effects on plasticity. In line with the gradient structure, the microhardness also presents a gradient. In general, the yield strength of a material can be expressed as [42]

$$\sigma_f=\sigma_0+kd_{fp}^{-1/2}+\alpha Gb\rho^{1/2} \quad (3)$$

where σ_f is the strength, σ_0 is the frictional stress, k is the Hall−Petch constant, d_{fp} is the mean free path of dislocations, α is a constant, and G is the shear modulus. According to Eq. (3), the strength increases with rising dislocation density and decreasing d_{fp}. Due to the repeated impact of high-energy and high-speed Al_2O_3 particles, SFPB treatment causes high strain rate plastic deformation on the alloy surface, which significantly increases the dislocation density and reduces d_{fp}, especially in the surface layer (Fig. 7). This causes lattice

distortion, resulting in the formation of high-amplitude CRS on the surface of the material. At the same time, the surface grain is refined to the nanometer level, forming a fine grain strengthening mechanism.

In addition, the intensity of this enhancement is also associated with high CRS after SFPB treatment. Studies have shown that residual tensile stress can accelerate the initiation of microcracks on the material surface, and reduce the fatigue life and overall surface integrity of the material [43]. However, CRS can redistribute the stress generated during tensile loading to the subsurface layer [44]. This counteracts the tensile stress on the surface layer where cracks normally generate, thus inhibiting crack formation. CRS can also promote the closure of cracks, thereby increasing the strength of the material. However, the prolonged impact time and intense gas pressure, such as 1.0 MPa for 90 s or 1.5 MPa for 60 s (Figs. 2(d, g)), weaken the ultimate tensile strength and yield strength by introducing surface microcracks. These cracks can act as traps for concentrated stress, causing actual local stress to far exceed the nominal level [29]. This makes the microcracks prone to further instability and expansion, ultimately leading to a substantial reduction in the strength of the material. At a gas pressure of 1.0 MPa and an impact time of 120 s, the strength of SFPB treated alloy is further reduced, and more and wider cracks appear on the surface (Fig. 2(e)).

In addition to strength, plasticity is another important mechanical property. Generally, coarse-grained materials have relatively low strength but high plasticity, while the strength of nanocrystalline materials is increased at the expense of plasticity [10]. The SFPB-induced gradient structure is an excellent strategy to overcome the strength−plasticity tradeoff. This is facilitated by the inhomogeneous distribution of strain within the gradient structure, which creates geometrically necessary dislocations that contribute to the formation of back stress reinforcement [45] and strengthening [46]. During deformation, different properties of fine surface grains and coarse internal matrix inhibit strain localization and early yielding [8,47], thus improving plasticity. In addition, WU et al [48] demonstrated that optimizing the gradient structure or the depth or proportion of the hardened layer can improve plasticity by selecting suitable surface treatment methods or parameters. When SFPB parameters (i.e. gas pressure and impact time) are not optimized, the strength of SFPB decreases, as shown in Fig. 10; when the gas pressure is 1.0 MPa and the impact time is greater than 60 s, the strength decreases.

5 Conclusions

(1) SFPB effectively induces the gradient nanostructure on the Ni−W−Co−Ta MHA surface. The increase of gas pressure and the increase of impact time both contribute to the decrease of surface particle size. At 1.0 MPa and 120 s, the minimum grain size is refined to 11.67 nm.

(2) Increasing the gas pressure and impact time deepens the deformation layer and increases the surface hardness. The depth of the deformation layer is extended to about 29 μm, and the surface microhardness reaches HV 451 when the gas pressure of 1.0 MPa and the impact time of 120 s are applied. SFPB has little effect on elongation. However, the fracture morphology of the alloy changes from ductile fracture to a mixture of ductile−brittle fracture.

(3) The best combination of strength and ductility is achieved at 1.0 MPa and 60 s. Under this condition, the minimum surface roughness is 6.25 μm, the maximum CRS reaches 988 MPa, and the peak ultimate tensile strength and yield strength reach 1236 MPa and 758 MPa, respectively, which are 22.5% and 38.8% higher than those of solid solution treated alloy, respectively. Excessive gas pressure and impact time cause surface micro-cracks, resulting in a decrease in strength and CRS.

CRediT authorship contribution statement

Yi XIONG: Conceptualization, Methodology, Writing − Original draft, Formal analysis, Resources, Visualization; **Miao-miao YANG:** Conceptualization, Software, Validation, Writing − Review & editing, Investigation; **Nan DU:** Conceptualization, Methodology, Validation, Resources; **Yong LI:** Methodology, Validation, Formal analysis, Resources; **Jin-jin TANG:** Formal analysis, Investigation, Data curation; **Kang-hao SHU:** Resources, Writing − Review & editing, Visualization; **Shu-bo WANG:** Investigation, Data curation; **Feng-zhang REN:** Supervision.

Declaration of competing interest

The authors declare that they have no known competing financial interests or personal relationships that could have appeared to influence the work reported in this paper.

Acknowledgments

This work was supported by the National key Research and Development Program of China (No. 2022YFB3705200), the National Natural Science Foundation of China (Nos. U1804146, 51905153, 52111530068), the Science and Technology Innovation Team Project of Henan University of Science and Technology, China (No. 2015XTD006), and the Major Science and Technology Project of Henan Province, China (No. 221100230200).

References

[1] DURLU N, ÇALIŞKAN N K, BOR S. Effect of swaging on microstructure and tensile properties of W−Ni−Fe alloys [J]. International Journal of Refractory Metals and Hard Materials, 2014, 42: 126−131.

[2] KIRAN U R, KUMAR J, KUMAR V, SANKARAN-ARAYANA M, RAO G N, NANDY T K. Effect of cyclic heat treatment and swaging on mechanical properties of the tungsten heavy alloys [J]. Materials Science and Engineering: A, 2016, 656: 256−265.

[3] HU Ke, LI Xiao-qiang, AI Xuan, QU Sheng-guan, LI Yuan-yuan. Fabrication, characterization, and mechanical properties of 93W−4.9Ni−2.1Fe/95W−2.8Ni−1.2Fe−1Al_2O_3 heavy alloy composites [J]. Materials Science and Engineering: A, 2015, 636: 452−458.

[4] XIONG Yi, SHU Kang-hao, LI Yong, CHEN Zheng-ge, ZHA Xiao-qin, HE Tian-tian, WANG Shu-bo. Excellent strength−ductility synergy in a ultra-high strength Ni−W−Co−Ta medium-heavy alloy by orthogonal rolling [J]. Journal of Materials Processing Technology, 2023, 316: 117968.

[5] YE Lei, HAN Yong, FAN Jing-lian, DU Zhi-yuan. Fabrication of ultrafine-grain and great-performance W−Ni−Fe alloy with medium W content [J]. Journal of Alloys and Compounds, 2020, 846: 156237.

[6] LI Y, LIU G Q, HU X B, WU L H, TAN C W, DRAVID V P, LIU S Z. A novel medium heavy alloy (MHA) with excellent static/dynamic properties and impact toughness [J]. Scripta Materialia, 2019, 162: 311−315.

[7] LI Yong, XIONG Yi, MA Yun-fei, HAN Shun, HE Tian-tian, WANG Chun-xu, REN Feng-zhang, WANG Shu-bo. Effect of aging treatment on the microstructure and properties of a novel medium-heavy NiWCoTa alloy subjected to pre-deformation [J]. Journal of Materials Engineering and Performance, 2023, 32(18): 8314−8324.

[8] LU K. Making strong nanomaterials ductile with gradients [J]. Science, 2014, 345(6203): 1455−1456.

[9] MA E, WU X L. Tailoring heterogeneities in high-entropy alloys to promote strength-ductility synergy [J]. Nature Communications, 2019, 10(1): 5623.

[10] SHAO C W, ZHANG P, ZHU Y K, ZHANG Z J, TIAN Y Z, ZHANG Z F. Simultaneous improvement of strength and plasticity: Additional work-hardening from gradient microstructure [J]. Acta Materialia, 2018, 145: 413−428.

[11] FANG T H, LI W L, TAO N R, LU K. Revealing extraordinary intrinsic tensile plasticity in gradient nano-grained copper [J]. Science, 2011, 331(6024): 1587−1590.

[12] WEI Yu-jie, LI Yong-qiang, ZHU Lian-chun, LIU Yao, LEI Xian-qi, WANG Gang, WU Yan-xin, MI Zhen-li, LIU Jia-bin, WANG Hong-tao, GAO Hua-jian. Evading the strength−ductility trade-off dilemma in steel through gradient hierarchical nanotwins [J]. Nature Communications, 2014, 5(1): 3580.

[13] MAUREL P, WEISS L, BOCHER P, GROSDIDIER T. Effects of SMAT at cryogenic and room temperatures on the kink band and martensite formations with associated fatigue resistance in a β-metastable titanium alloy [J]. Materials Science and Engineering: A, 2021, 803: 140618.

[14] DAS T, ERDOGAN A, KURSUNCU B, MALEKI E, UNAL O. Effect of severe vibratory peening on microstructural and tribological properties of hot rolled AISI 1020 mild steel [J]. Surface and Coatings Technology, 2020, 403: 126383.

[15] CHEN Xu-dong, LI Yu-sheng, ZHU Yun-tian, CHEN Yue-feng, YANG Bin. Layer-by-layer corrosion behavior of 316LN stainless steel with a gradient-nanostructured surface [J]. Electrochemistry Communications, 2020, 110: 106642.

[16] LIU Cheng-song, LIU Dao-xin, ZHANG Xiao-hua, AO Ni, XU Xing-chen, LIU Dan, YANG Jing. Fretting fatigue characteristics of Ti−6Al−4V alloy with a gradient nanostructured surface layer induced by ultrasonic surface rolling process [J]. International Journal of Fatigue, 2019, 125: 249−260.

[17] WANG Gao-qi, WANG Shou-ren, YANG Xue-feng, WEN Dao-sheng, GUO Yu. Microstructure, mechanical properties and fretting corrosion wear behavior of biomedical ZK60 Mg alloy treated by laser shock peening [J]. Transactions of Nonferrous Metals Society of China, 2023, 33(6): 1715−1728.

[18] ZHU Wen-guang, MA Chi, ZHANG Cong-hui, HU Kun, ZENG Xiang-kang. Fatigue crack propagation behavior in Ti−6Al−4V alloy with surface gradient structure fabricated by high-energy shot peening [J]. Transactions of Nonferrous Metals Society of China, 2023, 33(10): 3003−3016.

[19] YUAN Kui-lin, SUMI Y. Simulation of residual stress and fatigue strength of welded joints under the effects of ultrasonic impact treatment (UIT) [J]. International Journal of Fatigue, 2016, 92: 321−332.

[20] JIN Lei, CUI Wen-fang, SONG Xiu, LIU Gang, ZHOU Lian. Effects of surface nanocrystallization on corrosion resistance of β-type titanium alloy [J]. Transactions of Nonferrous Metals Society of China, 2014, 24(8): 2529-2535.

[21] LUO Si-hai, ZHOU Liu-cheng, WANG Xue-de, CAO Xin, NIE Xiang-fan, HE Wei-feng. Surface nanocrystallization and amorphization of dual-phase TC11 titanium alloys under laser induced ultrahigh strain-rate plastic deformation [J]. Materials (Basel), 2018, 11(4): E563.

[22] ZHANG Chao-yi, DONG Ya-lin, YE Chang. Recent

developments and novel applications of laser shock peening: A review [J]. Advanced Engineering Materials, 2021, 23(7): 2001216.

[23] MA Guo-zheng, XU Bin-shi, WANG Hai-dou, SI Hong-juan. Effects of surface nanocrystallization pretreatment on low-temperature ion sulfurization behavior of 1Cr18Ni9Ti stainless steel [J]. Applied Surface Science, 2010, 257(4): 1204−1210.

[24] ZHANG Liu-yan, MA Ai-bin, JIANG Jing-hua, SONG Dan, YANG Dong-hui, CHEN Jian-qing. Electrochemical corrosion properties of the surface layer produced by supersonic fine-particles bombarding on low-carbon steel [J]. Surface and Coatings Technology, 2013, 232: 412−418.

[25] MA Guo-zheng, XU Bin-shi, WANG Hai-dou, SI Hong-juan, YANG Da-xiang. Effect of surface nanocrystallization on the tribological properties of 1Cr18Ni9Ti stainless steel [J]. Materials Letters, 2011, 65(9): 1268−1271.

[26] LI Yang, LIAN Yang, LI Jing-kai, HE Tian-tian, ZOU Yun. Effect of supersonic fine particle bombardment on the surface integrity and wear performance of DZ2 axle steel [J]. Surface and Coatings Technology, 2022, 435: 128250.

[27] ZHANG Bao-sen, DONG Qiang-sheng, BA Zhi-xin, WANG Zhang-zhong, SHI Han-cheng, XUE Yan-ting. Tribological properties of surface-textured and plasma-nitrided pure titanium under oil lubrication condition [J]. Journal of Materials Engineering and Performance, 2018, 27: 186−193.

[28] ZHANG Yu-xiang, YANG Jian-hai, GE Li-ling, ZHANG Xin, CHEN Jia-zhao. Research on mechanism of surface nanocrystalline layer in 2219 Al alloy induced by supersonic fine particles bombarding [J]. International Journal of Engineering Research in Africa, 2016, 24: 1−8.

[29] ZHOU Tian, XIONG Yi, CHEN Zheng-ge, ZHA Xiao-qin, LU Yan, HE Tian-tian, REN Feng-zhang, SINGH H, KÖMI J, HUTTULA M, CAO Wei. Effect of surface nano-crystallization induced by supersonic fine particles bombarding on microstructure and mechanical properties of 300M steel [J]. Surface and Coatings Technology, 2021, 421: 127381.

[30] WU Yong-li, XIONG Yi, CHEN Zheng-ge, LIU Wei, ZHANG Xin, WANG Shu-bo, CAO Wei. Effect of gas pressure on the microstructure and mechanical properties of TC11 titanium alloy during supersonic fine particle bombardment [J]. Transactions of Nonferrous Metals Society of China, 2023, 33(8): 2379−2394.

[31] CHEN Xue-peng, ZHANG Ling-feng, XIONG Yi, YAO Huai, REN Feng-zhang, ZHANG Jing. Effects of supersonic fine particle bombardment on the microstructure and corrosion properties of Ti−6Al−3Nb−2Zr−1Mo alloy [J]. Surface and Coatings Technology, 2023, 459: 129383.

[32] BAG A, LÉVESQUE M, BROCHU M. Effect of shot peening on short crack propagation in 300M steel [J]. International Journal of Fatigue, 2020, 131: 105346.

[33] CHEN Ming, JIANG Chuan-hai, XU Zhou, ZHAN Ke, JI V. Experimental study on macro- and microstress state, microstructural evolution of austenitic and ferritic steel processed by shot peening [J]. Surface and coatings technology, 2019, 359: 511−519.

[34] YANG C, LI M Q, LIU Y G. Further refinement mechanisms of nanograins in nanocrystalline surface layer of TC17 subjected to severe plastic deformation [J]. Applied Surface Science, 2021, 538: 147941.

[35] GHOSH S, BIBHANSHU N, SUWAS S, CHATTERJEE K. Surface mechanical attrition treatment of additively manufactured 316L stainless steel yields gradient nanostructure with superior strength and ductility [J]. Materials Science and Engineering: A, 2021, 820: 141540.

[36] HUANG Shu, YUAN Guang, SHENG Jie, TAN Wen-sheng, AGYENIM-BOATENG E, ZHOU Jian-zhong, GUO Hua-feng. Strengthening mechanism and hydrogen-induced crack resistance of AISI 316L stainless steel subjected to laser peening at different power densities [J]. International Journal of Hydrogen Energy, 2018, 43(24): 11263−11274.

[37] LIU Wen-bo, JIN Xiao, ZHANG Bo, YUN Di, CHEN Pi-heng. A coupled EBSD/TEM analysis of the microstructure evolution of a gradient nanostructured ferritic/martensitic steel subjected to surface mechanical attrition treatment [J]. Materials, 2019, 12(1): E140.

[38] JIANG He, DONG Jian-xin, ZHANG Mai-cang, YAO Zhi-hao. A study on the effect of strain rate on the dynamic recrystallization mechanism of alloy 617B [J]. Metallurgical and Materials Transactions A, 2016, 47: 5071−5087.

[39] XIONG Yi, SHU Kang-hao, LI Yong, CHEN Zheng-ge, ZHA Xiao-qin, HE Tian-tian, HAN Shun, WANG Chun-xu. Deformation temperature impacts on the microstructure evolution and mechanical properties of a novel medium-heavy alloy (MHA) [J]. Materials Science and Engineering: A, 2022, 856: 144005.

[40] XU Yun-hua, FANG Liang, CEN Qi-hong, ZHU Jin-hua. Nano structure and transformation mechanism of white layer for AISI 1045 steel during impact wear [J]. Wear, 2005, 258(1/2/3/4): 537−544.

[41] BAGHERIFARD S, SLAWIK S, FERNÁNDEZ-PARIENTE I, PAULY C, MÜCKLICH F, GUAGLIANO M. Nanoscale surface modification of AISI 316L stainless steel by severe shot peening [J]. Materials & Design, 2016, 102: 68−77.

[42] LIU Dan, LIU Dao-xin, ZHANG Xiao-hua, LIU Cheng-song, AO Ni. Surface nanocrystallization of 17-4 precipitation-hardening stainless steel subjected to ultrasonic surface rolling process [J]. Materials Science &Engineering A, 2018, 726: 69−81.

[43] LUO Xian, REN Xue-ping, JIN Qi, QU Hai-tao, HOU Hong-liang. Microstructural evolution and surface integrity of ultrasonic surface rolling in Ti6Al4V alloy [J]. Journal of Materials Research and Technology, 2021, 13: 1586−1598.

[44] KIM J C, CHEONG S K, NOGUCHI H. Evolution of residual stress redistribution associated with localized surface microcracking in shot-peened medium-carbon steel during fatigue test [J]. International Journal of Fatigue, 2013, 55: 147−157.

[45] WU Xiao-lei, ZHU Yun-tian. Heterogeneous materials: A new class of materials with unprecedented mechanical properties [J]. Materials Research Letters, 2017, 5(8): 527−532.

[46] YANG Mu-xin, PAN Yue, YUAN Fu-ping, ZHU Yun-tian, WU Xiao-lei. Back stress strengthening and strain hardening in gradient structure [J]. Materials Research Letters, 2016, 4(3): 145−151.

[47] WU Xiao-lei, YANG Mu-xin, YUAN Fu-ping, WU Gui-lin, WEI Yu-jie, HUANG Xiao-xu, ZHU Yun-tian, Heterogeneous lamella structure unites ultrafine-grain strength with coarse-grain ductility [J]. Proceedings of the National Academy of Sciences, USA, 2015, 112(47): 14501−14505.

[48] WU X L, JIANG P, CHEN L, ZHANG J F, YUAN F P, ZHU Y T. Synergetic strengthening by gradient structure [J]. Materials Research Letters, 2014, 2(4): 185−191.

超音速微粒轰击诱导梯度纳米结构对 Ni−W−Co−Ta 高密度合金显微组织和性能的影响

熊 毅[1,2]，杨苗苗[1]，杜 楠[3]，厉 勇[4]，汤金金[1]，舒康豪[5]，王树泊[6]，任凤章[1]

1. 河南科技大学 材料科学与工程学院，洛阳 471023；
2. 有色金属新材料与先进加工技术省部共建协同创新中心，洛阳 471023；
3. 洛阳光电技术发展中心，洛阳 471003；
4. 钢铁研究总院有限公司 特殊钢研究院，北京 100081；
5. 中信重工机械股份有限公司，洛阳 471039；
6. Nano and Molecular Systems Research Unit, University of Oulu, Oulu, FIN-90014, Finland

摘 要：系统研究超音速微粒轰击(SFPB)诱导梯度纳米结构对 Ni−W−Co−Ta 高密度合金表面完整性、显微组织演变及力学性能的影响。结果表明：SFPB 处理能在 Ni−W−Co−Ta MHA 表层形成梯度纳米结构。当气体压力为 1.0 MPa、冲击时间为 60 s 时，合金的极限抗拉强度和屈服强度分别达到最大值 1236 MPa 和 758 MPa，相比固溶态合金的提高了 22.5%和 38.8%，伸长率(46.3%)与固溶态合金的接近，此时，合金具有最佳的强度和塑性匹配。然而，当气体压力过大或冲击时间过长时，试样表面出现微裂纹，在残余应力发生一定程度松弛的同时强度下降。形变层深度和表面显微硬度随着冲击时间的延长及气体压力的增大逐渐增大，在 1.0 MPa 及 120 s 时分别达到最大值 29 μm 和 HV 451，表层晶粒则细化至最小值 11.67 nm。经 SFPB 处理后 Ni−W−Co−Ta MHA 的伸长率变化不大，断裂方式由处理前的韧性断裂转变为处理后的韧、脆混合断裂。

关键词：超音速微粒轰击；梯度纳米结构；Ni−W−Co−Ta 高密度合金；显微组织；力学性能

(Edited by Wei-ping CHEN)